In Operando Optical Tracking of Oxygen Vacancy Migration and Phase Change in few Nanometers Ferroelectric HZO Memories

Atif Jan, Thomas Rembert, Sunil Taper, Joanna Symonowicz, Nives Strkalj, Taehwan Moon, Yun Seong Lee, Hagyoul Bae, Hyun Jae Lee, Duk-Hyun Choe, Jinseong Heo, Judith MacManus-Driscoll, Bartomeu Monserrat, and Giuliana Di Martino*

Ferroelectric materials offer a low-energy, high-speed alternative to conventional logic and memory circuitry. Hafnia-based films have achieved single-digit nm ferroelectricity, enabling further device miniaturization. However, they can exhibit nonideal behavior, specifically wake-up and fatigue effects, leading to unpredictable performance variation over consecutive electronic switching cycles, preventing large-scale commercialization. The origins are still under debate. Using plasmon-enhanced spectroscopy, a non-destructive technique sensitive to <1% oxygen vacancy variation, phase changes, and single switching cycle resolution, the first real-time in operando nanoscale direct tracking of oxygen vacancy migration in 5 nm hafnium zirconium oxide during a pre-wake-up stage is provided. It is shown that the pre-wake-up leads to a structural phase change from monoclinic to orthorhombic phase, which further determines the device wake-up. Further migration of oxygen ions in the phase changed material is then observed, producing device fatigue. These results provide a comprehensive explanation for the wake-up and fatigue with Raman, photoluminescence and darkfield spectroscopy, combined with density functional theory and finite-difference time-domain simulations.

A. Jan, T. Rembert, S. Taper, J. Symonowicz, N. Strkalj,
J. MacManus-Driscoll, B. Monserrat, G. Di Martino
Department of Materials Science and Metallurgy
University of Cambridge
Cambridge CB3 0FS, UK
E-mail: gd392@cam.ac.uk
T. Moon
Department of Electrical and Computer Engineering
University of Southern California
Los Angeles 90089, USA
Y. S. Lee, H. J. Lee, D.-H. Choe, J. Heo
Samsung Advanced Institute of Technology
Suwon-si 16678, South Korea
H. Bae
Department of Electronics Engineering
Jeonbuk National University
Jeonju-si 54896, South Korea

The ORCID identification number(s) for the author(s) of this article can be found under https://doi.org/10.1002/adfm.202214970.

1. Introduction

Ferroelectric (FE) thin films, exhibiting spontaneous and controllable out-of-plane polarization states, offer a unique non-volatile digital memory platform due to their field-based switching mechanism and state retention.[1,2] FE random access memory (FeRAM) is a promising technology due to low power and high-speed switching and long device lifetime.[3–6] Moreover, multi-state behavior has been achieved for applications in neuromorphic computing.[7–9] Early FE research focused on oxide perovskite structures; however, recent advances have rendered doped binary oxides like $Hf_{0.5}Zr_{0.5}O_2$ (HZO) more desirable for ultrathin microelectronics.[10–19] Despite existing implementations of FEs into the state-of-the-art electronics, the underlying physics of phenomena like wake-up and fatigue remain unclear. These effects alter the remanent polarization value of a device (i.e., increasing during wake-up and decreasing during fatigue), causing the expected device performance to vary over consecutive electronic switching cycles.[20] Although, oxygen vacancy (Vo) migration has been proposed to induce phase change upon electric field cycling[21–27] and previous works had drawn a relation between structural changes and wake-up/fatigue,[24,28–30] the understanding of those phenomena remains highly fragmentary, incomplete and often contradictory. Studies in[24,28] mention the importance of Vo in enhanced FE switching, but no proof of Vo movement is provided. EXAFS studies had shown Vo motion leading to wake-up, but with no phase change being observable by XRD.[29] On the other hand, wake up and fatigue had been tied up to structural changes and phase change at the electrode interface, respectively, but the role of Vo has not been considered.[30] Furthermore, existing probing techniques are either destructive,[27] preventing in operando studies, and often only providing aggregate information over an area much larger than the localized nanoscale effects.[31] In general, there is great need for in situ nano-kinetics studies toward underpinning phenomenon like wake-up and fatigue.
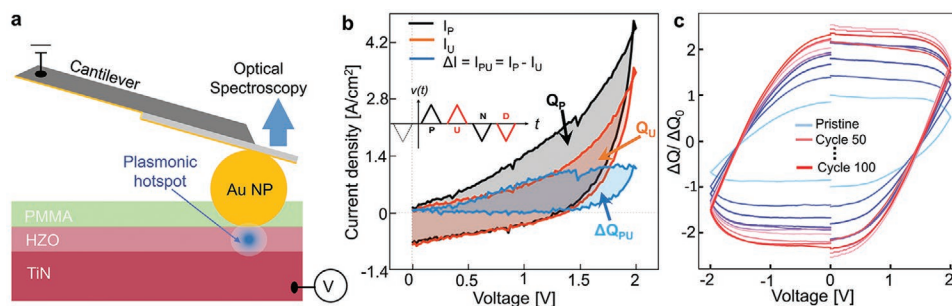
Figure 1. FeRAM contacting scheme. a) Simultaneous electrical contact and optical detection for AuNP/HZO/TiN devices, with plasmonic field tightly confined in the HZO spacer material. A transparent but electrically conductive cantilever ensures bias through individual Au NPs, while PMMA insulates the rest of the device. b) Current densities for P and U pulses (I_P and I_U) of a PUND biasing scheme and remanent charge difference ($\Delta Q = Q_P - Q_U$). Similar polarization -state-induced behavior is seen for the negative voltage sweeps. c) Typical ΔQ-V loops show pristine (light blue), wake-up (blue-to-pink), and fatigue (pink-to-red) cycles.

2. Results and Discussion

Our study, through Raman, photoluminescence (PL), and real-time dark-field (DF) spectroscopies, tackles exactly those issues and is able to unveil the intricate interplay between Vo movement and phase transitions, unequivocally proving them responsible for wake-up and fatigue.

Large optical field enhancements in nanoplasmonic systems have been proven to be useful to non-destructively detect the evolution of Vo migration[32] in the resistive switching mechanism.[32–34] Similarly, here, we use a Nanoparticle-on-Mirror (NPoM) geometry, where the film is electrically contacted as a two-terminal device via a top gold nanoparticle (AuNP) and underlying conductive ("plasmonic") mirror film (**Figure 1**a,b). Surface-Enhanced Raman (SERS), photoluminescence, and white light scattering spectra are then plasmonically enhanced highlighting the – otherwise undetectable – morphology changes happening in just 5 nm thick FE HZO film, while its polarization state changes through electrical cycling.

2.1. Material Characterization

The crystalline structure of the 5 nm thick HZO films before and after annealing is characterized by X-ray diffraction (Experimental Section) in a grazing incidence geometry (GIXRD) with a fixed incident angle of 0.7° while scanning the detector from 20° to 80° in 2θ (Figure S1, Supporting Information). Two-terminal devices (Figure 1a) with drop-casted AuNP as top contacts, an active layer of 5 nm FE HZO, and 100 nm of TiN bottom contact resulting in an AuNP/HZO/TiN metal-insulator-metal (MIM) structure was prepared (Experimental Section). TiN as the bottom electrode sustains plasmonically coupled modes in the nanocavity between AuNP and itself.[32,35,36] Additionally, TiN promotes FE phase formation due to oxygen scavenging.[37] Individual 80 nm AuNPs are contacted via a flexible, electrically conductive, and optically transparent cantilever (Experimental Section). The localized plasmons of each AuNP couple to their image charges in the TiN film underneath the HZO spacer layer, forming a confined plasmonic hotspot, similar to a nanoparticle dimer (Figure 1a). A 60 nm PMMA layer insulates the cantilever from contacting the entire HZO, leaving 20 nm of

exposed AuNP for electrical contact (Figure 1a) (Figure S2, S3, Supporting Information).

2.2. Electrical Characterization

For FE HZO films, coercive and breakdown fields are $E_C \approx 1.8$ MV cm^{-1} and $E_{BD} \approx 5$–8 MV cm^{-1}, respectively, with the breakdown field a function of cycling frequency.[21,38] Thus, we sweep between −2 and+2 V, resulting in a maximum field of 4 MV cm^{-1}, sufficiently above E_C and below E_{BD}.

PUND voltage profiles[39] discriminate the contributions of FE switching from resistive-like leakage effects (Experimental Section). The current profiles of each section of the PUND stimulus clearly show the difference in current magnitudes between HZO polarization states (Figure 1c). However, because of the dynamic nature of V_O migration within the HZO layer, the PUND measurement does not fully compensate for leakage currents. The nm-sized top contact restricts the current flowing through our device to ≈pA, therefore necessitating a low-noise Source-Measure Unit (SMU) measuring current at slow speeds (Experimental Section). The slow speed (≈1 Hz) compared to conventional ones (100 Hz–10 kHz) results in an overestimation of polarization.[39] Moreover, given the highly asymmetric nature of the NPoM device structure it is challenging to define a "true" device area, hence, we chose to represent internal changes in the HZO as a function of charge variation rather than an absolute polarization value. Therefore, current differences (e.g., $I_P - I_U$ and $I_N - I_D$) are integrated over the measurement duration to quantify the change in internal charge within the film between polarization states (ΔQ, remanent polarization) and normalized to the remanent polarization of the initial PUND measurement (ΔQ_0). This results in a change in polarization charge ($\Delta Q / \Delta Q_0$) representing internal charge, hence, polarization change, within the HZO films after sequential measurements (Figure 1b). Because each PUND polarity (e.g., PU for +2 V, ND for −2 V) is performed and integrated separately, we have chosen to center each half around the origin for ease of visualization. Over continued cycling, a wake-up-like effect is observed, exhibiting a nearly 2.5x increase in remanent polarization, comparable to the remanent polarization changes during wake-up reported in similar films.[20,40] Such behavior

can be seen within the first 100 cycles due to the slow nature of the measurement (≈1 Hz) compared to conventional FE characterization speeds (≈100 Hz–10 kHz).[21] Furthermore, NP deposition is a random process on the nm scale, and different cycling speeds are required for various optical characterizations (Raman, PL, and DF), so wake-up and fatigue might happen at varying times.

2.3. In Situ Raman and Photoluminescence

Wake-up and fatigue in ultra-thin HZO have been widely discussed in the literature and broadly attributed to polar phase formation and oxygen voltammetry across the electrodes.[27] As we show below, the new information from this work is a key direct proof the wake-up and fatigue result from oxygen motion and phase transition within the HZO films. Our SERS shows the presence of monoclinic (380,[41] 510,[42] and 600 cm^{-1}[43] peaks), tetragonal (680[41] and 820 cm^{-1}[43] peaks), and orthorhombic (335[43] and 740 cm^{-1}[41]) phases, before and after cycling (**Figure 2**a).

Over 1000 cycles, an increase of 108% in the area under o-phase at 335 cm^{-1} and a 13% increase at 740 cm^{-1} is observed. A modest rise in the t-phase area of 18.6% near 680 cm^{-1} and an appreciable 12.7% decrease in the area under m-peak near 510 cm^{-1} is observed. The corresponding polarization charge (Figure 2a, inset) shows the film has run through the wake-up stage and entered fatigue. For the first time, SERS confirms a change in the morphology in just 5 nm thick HZO, with an increase in o/t-phase and a decrease in m-phase. It has been suggested that the o-phase can be achieved from the t-phase primarily due to their structural similarities,[44] while due to oxidation of TiN, the metastable t-phase could be stabilized over the m-phase in the presence of oxygen vacancies.[41] Although SERS confirms a definite change in morphology, further research was necessary to better understand the causes of this phase transition, that is, the role of vacancies and defects.[29]

Our PL aims to shed light onto the relation between field cycling and the phase transitions. We collect a discrete number of PL spectra over device lifetime (Experimental Section),

hence tracking oxygen evolution over cycling. We observe two luminescence peaks at 565 and 660 nm (Figure 2b), previously shown to be strongly correlated with oxygen reduction in the film.[45] In the pristine state, a small luminescence peak ≈660 nm indicates a Vo defect state (Figure 2b, cyan). Cycling the device leads to its appreciable intensity increase, together with new emission at ≈565 nm (Figure 2b, blue). Electrically, this event initiates the wake-up, visible as an increase in $\pm\Delta Q/\Delta Q_0$ near cycle 800 (Figure 1b, inset). After wake-up, the PL intensity reverts to a defective-free film (Figure 2b, pink). In fact, the monoclinic phase is not the ground state under the presence of oxygen vacancies with a concentration ≈6%.[46] Our results prove an increase of defect states in a pre-wake-up stage, ultimately leading to the FE-orthorhombic phase, demonstrating the decisive role of oxygen vacancies in the FE appearance in HZO.

2.4. In Situ Darkfield Spectroscopy

Though SERS and PL are conclusive, they only represent a snapshot of film morphology at discrete instances of field cycling. To finely (to the single cycle) visualize the dynamics of wake-up and fatigue in real-time, we therefore devise an in operando tracking of atomistic changes within FE ultrathin films based on plasmon-enhanced DF spectroscopy.

The optical response of this system was measured by illuminating the sample with a white-light beam incident at 60° and collecting the scattered light through a dark-field objective (Experimental Section). A representative polarization charge evolution upon cycling is shown in **Figure 3**a. The simultaneous tracking of scattering signal shows strong peaks at $\lambda_1 \approx 520$ nm, $\lambda_2 \approx 650$ nm, and $\lambda_3 \approx 830$ nm, corresponding to multiple resonances or gap modes supported by the thin plasmonic "cavity" formed between the lower Au NP facet and the "mirror" TiN surface.[47] The resonant wavelength and intensity of these plasmonic peaks are highly sensitive to conductivity and refractive index change of the HZO layer. In fact, during the first 50 cycles, we observe an intensity decrease for λ_2, and intensity increase for λ_3, with a blueshift of both peaks. The corresponding electrical trace ($\pm\Delta Q/\Delta Q_0$ remanent polarization) is unchanged (Figure 3a),
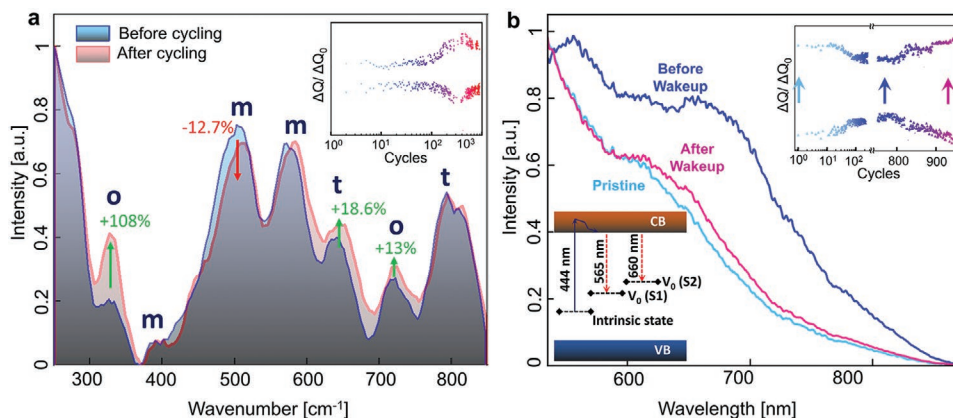

Figure 2. SERS and photoluminescence from NPoM geometry. a) SERS spectrum of AuNP/HZO/TiN device before (blue) and after (red) cycling with relative polarization charge (ΔQ) evolution over 10^3 cycles (inset). b) PL spectra of pristine device (cyan), before (blue), and after (pink) wake-up with relative polarization charge (ΔQ) evolution over 10^3 cycles (top insets) and possible optical transitions involving Vo defect states (bottom inset).
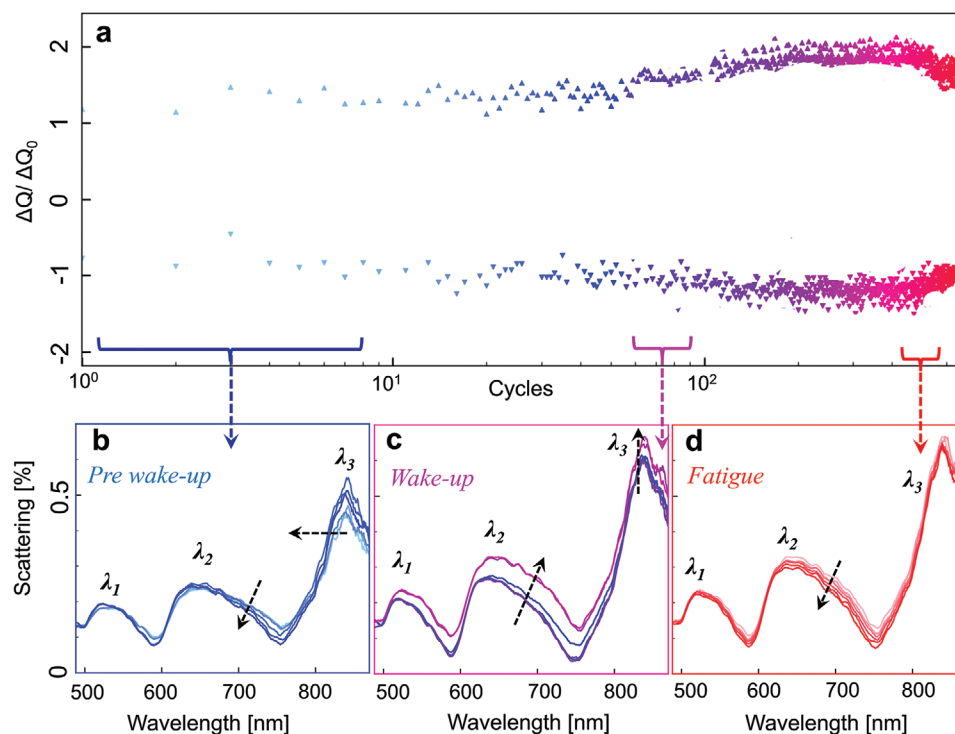
Figure 3. In operando DF scattering showing pre-wake-up, wake-up, and fatigue. a) Polarization charge ($\pm\Delta Q/\Delta Q_0$) evolution over 700 cycles for a AuNP/HZO/TiN and corresponding DF scattering spectra collected during pre-wake-up b), wake-up c), and fatigue d). Resonant plasmonic peaks are visible at $\lambda_1 \approx 530$ nm, $\lambda_2 \approx 650$ nm, and $\lambda_3 \approx 830$ nm. λ_2 reduces its intensity and blueshifts (pre-wake-up), then increases its intensity and redshifts (wake-up) and finally again reduces its intensity and blueshifts (fatigue). λ_3 blueshifts (pre-wake-up) and increases in intensity during wake-up, however no appreciable change is noticed during fatigue.

showing how our optical technique is able to highlight mechanism otherwise invisible to electrical characterization. For these cycles, we introduce the new term of "pre-wake-up". After 50 cycles, the phenomenon reverses. During cycle 60–110 (Figure 3c), the plasmon resonances associated with λ_2 grows in intensity, accompanied by noticeable redshift, accompanied by an increase in intensity for λ_3. Interestingly, during this stage the $\pm\Delta Q/\Delta Q_0$ polarization charge increases (remanent stored charge grows) to almost double that of the pristine measurement. Finally, fatigue is observed with continuous device cycling and the remanent polarization reduces after 550 cycles. The corresponding DF spectra between 550 and 610 cycles (Figure 3d) show a strong intensity decrease and a blueshift for λ_2, while λ_3 remains unchanged both in intensity and resonant wavelength. Similar behavior has been observed for AuNP/HZO/Au samples. Au, being a noble metal, is not as reactive to oxygen, and its vacancy-induced reaction is much weaker compared to TiN resulting in slightly different optical spectra. Therefore, the vacancy changes leading to wake-up are less pronounced on Au than on TiN, but the sustained cycling and spectral shifts indicating spectral shifts for fatigue are comparable (Figure S4, Supporting Information).

2.5. DFT and FDTD

To link the optical signatures observed experimentally with the various morphology regimes, we used a combination of density functional theory (DFT) calculations and finite-difference time-domain (FDTD) simulations (Experimental Section; Figure S5, S6 Supporting Information) to analyze how the plasmonic modes in HZO are influenced by Vo drift and phase change (from monoclinic to orthorhombic domains[24–27]). Both these effects are directly linked to changes in the index of refraction of HZO, which alters the plasmonic resonant peaks.[36] Previous work has used cantilever detection on NPoM structures, with the ability to track the motion of a few hundred Vo with nanometer-scale sensitivity in resistive switching materials.[32] Here, we further expand V_o migration-induced spectral shifts, including shifts occurring due to crystallographic phase change. We present a cycle-to-cycle explanation of the interplay between V_O migration and monoclinic-to-orthorhombic phase change to rationalize the wake-up and fatigue behavior measured in our 5 nm thick FE HZO films.

We model monoclinic HZO (m-HZO) and orthorhombic HZO (o-HZO) using a $2 \times 2 \times 2$ supercell containing 64 oxygen atoms. We then incorporate oxygen vacancies with a resultant 1.56% Vo concentration (1/64 in the supercell). We use DFT to evaluate the dielectric functions of the m-HZO and o-HZO defective phases and then from these calculate the corresponding refractive indices. Plasmon oscillations in the NP, perpendicular to the surface, induce image charges within the TiN mirror, confining the field within the gap and giving rise to the plasmon cavity modes. To parameterize the influence of Vo-rich/phase changed bridges on the spectral far-field response of the NPoM system, we incorporate refractive indices calculated
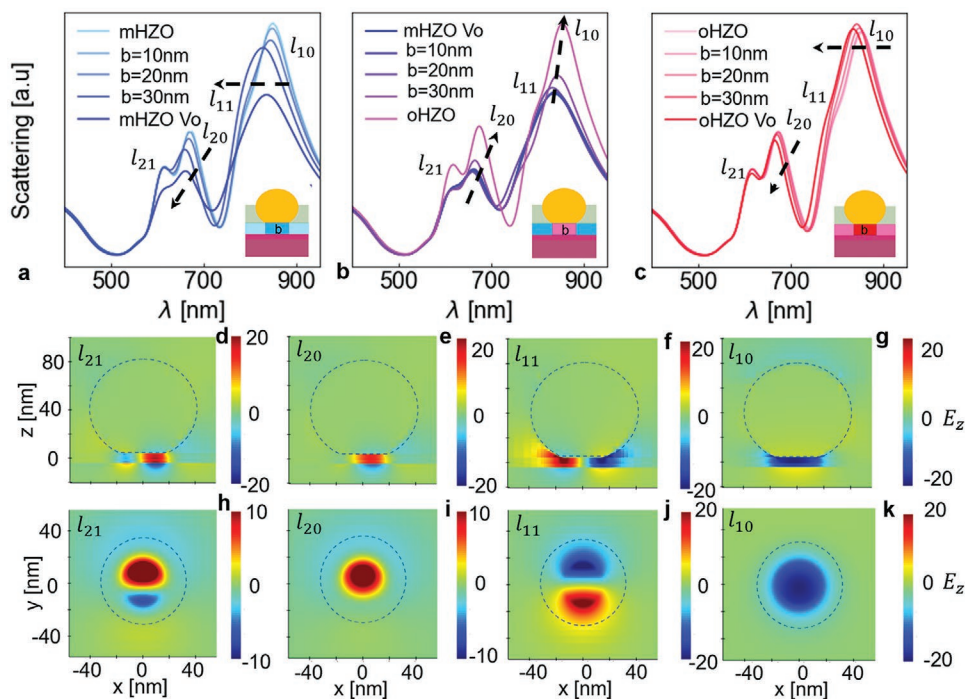
Figure 4. Numerical simulation of optical gap modes. FDTD simulation modes for 80 nm AuNP on HZO(5 nm)/TiO2(3 nm)/TiN(100 nm) and 60 nm PMMA coating with a) monoclinic Vo-rich bridge width b = 0, 10, 20, 30 nm and fully Vo-rich m-HZO, b) fully Vo-rich m-HZO hosting o-phase bridge width b = 0, 10, 20, 30 nm and fully o-HZO, c) orthorhombic Vo-rich bridge width b = 0, 10, 20, 30 nm and fully Vo-rich o-HZO. Insets: Geometry of the AuNP over the changing region. d–k) Field cuts of the l_{21}, l_{20}, l_{11}, and l_{10} modes taken over the mid-gap plane perpendicular (d–g) and parallel (h–k) to the substrate.

through DFT, into FDTD simulations. The diameter of the cylindrical monoclinic Vo-rich bridge varied from b = 0–30 nm, from no connection to fully Vo-rich m-HZO, giving the optical spectra shown in **Figure 4**a. A similar approach is used for describing the Vo-rich m-HZO to o-HZO transition (Figure 4b) and o-HZO to Vo-rich o-HZO (Figure 4c). The simulated scattering spectra (Figure 4a–c) are the result of first-order bright and dark modes l_{10} and l_{11} and second-order modes l_{20} and l_{21} within HZO (Figure 4d–k).

From our simulations, we thus conclude that changes to the experimentally observed λ_2 peak come from superposed l_{21} and l_{20} modes, while changes to the λ_3 peak come from superposed l_{10} and l_{11} modes. The intensity and peak position of the resonances is fairly consistent between the experiment and simulation. In fact, the l_{20} and $l_{10} + l_{11}$ modes intensities reduce and blueshift as oxygen vacancies are incorporated into the m-HZO supercell (Figure 4a). Then as Vo-rich m-HZO supercell turns into o-HZO, l_{20} and $l_{10} + l_{11}$ modes intensities increase and redshift (Figure 4b). Finally, the l_{20} and $l_{10} + l_{11}$ modes intensities decrease and blueshift as the o-HZO supercell turns into Vo-rich o-HZO (Figure 4c). The experimental trend observed for λ_2 (Figure 3a–c) strongly matches the l_{20} mode behavior (pre-wake-up with intensity reduction and blueshift, wake-up with intensity increase and redshift, fatigue with intensity reduction and blueshift), and the λ_3 peak shows a milder – but still visible – match with the $l_{10} + l_{11}$ modes (pre-wake-up with blueshift and wake-up with intensity increase), probably due to a reduced detection efficiency and a lower intensity of the light source closer to the IR region. Similar comparison was performed for AuNP/HZO/Au samples (Figure S7, Supporting Information). The vacancy induced o-phase is not to be misunderstood as morphologically defect free, but homogeneously distributed vacancies through the film. It must be noted however, that in the fatigue simulation, a Vo ortho bridge growing in a defect-free orthorhombic layer would behave similarly to a higher-concentration Vo bridge in a matrix with a distributed low vacancy concentration (Figure S8, Supporting Information).

3. Conclusion

In summary, we link the fields of nanoscale device engineering and plasmon-enhanced light-matter interactions to implement optically accessible FE memories. SERS confirms phase transition into o-HZO from a predominant m-HZO film upon field cycling, thus leading to more FE domains, and hence wake-up. This phase change is assisted by vacancy migration through the HZO film in a pre-wake-up stage, as confirmed by PL, showing the creation of Vo-related defect states and the associated emission peaks before wake-up. Furthermore, through our in operando plasmon enhanced DF spectroscopy, we can track in real-time, with single switching cycle resolution, the dynamic leading to wake-up and fatigue in FE HZO. The transitions in the optical signatures are rationalized by DFT and FDTD simulations.

**ADVANCED
SCIENCE NEWS**

www.advancedsciencenews.com

**ADVANCED
FUNCTIONAL
MATERIALS**

www.afm-journal.de

4. Experimental Section

Sample Preparation: Bottom electrodes were deposited onto (100)-oriented p++ Si wafers after a dilute hydrofluoric acid cleaning step. The Au-based wafer was first sputtered with 5 nm of TiN and then followed by 100 nm thermal evaporation of Au to form the bottom electrode, whereas the TiN-based wafer was sputtered with 100 nm of TiN in Ar 15 sccm/N_2 95 sccm atmosphere at room temperature. The 5 nm mixed-phase HZO films were then grown via atomic layer deposition (ALD) on both wafers, followed by 130 nm of sputtered Mo using 250 W gun power on a 5 inch target. This sputtering condition leaves less bombardment damage on the film. Wafers were then treated with a 30 s rapid thermal annealing step at 500 °C, followed by top contact UV lithography patterning and Mo etching for top contacts of test devices. For this study, Au nanoparticles (80 nm diameter AuNPs in citrate capping agent) from BBI Solutions were drop-cast on the bare HZO samples with no top contact. The AuNP colloid solution was diluted to allow for a density of $\approx 10^{-3}$ μm^{-2}. A 210 nm layer of poly(methyl methacrylate) (PMMA) was then spin-cast on the samples in two spinning steps and then subjected to a 3 min bake at 200 °C. This was followed by O_2 plasma etch to expose the top of the AuNPs for electrical contact. The final PMMA thickness was $\approx$60–90 nm, including sample variation, as measured by ellipsometry (J.A. Woollam EC-400, 75 W Xe light source) on Si dummy samples.

GIXRD Characterization: GIXRD measurements were performed using a Panalytical Empyrean diffractometer with a 1/32° divergence slit and programmable anti-scatter/receiving slits set at 1.5 mm.

Electrical Characterization: As a consequence of this device configuration's capacitor-like behavior and nanoscale top contact area (AuNP facet $d \approx$30 nm, $A_{contact} \approx$ 700 nm^2), a low-noise low current SMU was used for electrical probing of minute current values.[32–34] A Keithley 2634B source meter which allows for low noise measurement down to 10 pA, was used for electrical characterization with the two channels connected to the AuNP and underlying conductive film connected as ground and supply, respectively. Connections to the AuNPs were made through a triaxial link to a breakout wire connected to the conductive cantilever, with bottom electrode contacts made via a triaxial connection to a tungsten probe tip directly to the conductive film. The voltage sweep resolution directly controls sweep rates, $f \approx$ 1 Hz (voltage steps of V = 100 mV). The low frequency allowed the SMU to sense minimal currents from the nanoscale device size. Measurements were taken with a 100 nA measurement range and 1 nA current compliance. All measurements were performed at ambient conditions.

Optical Characterization: Raman spectroscopy was performed using a CW single-longitudinal-mode 633 nm laser from Integrated Optics. The power on the sample was 1.5 µW. The Raman signal was collected through optics purchased from Thorlabs into a Andor Kymera 328i spectrometer coupled to a Newton EMCCD camera from Oxford Instruments.

Photoluminescence was performed using CW 444 nm laser from Integrated optics. The signal was sent through an optical fiber QP50-2-UV–vis to Oceans Optics QE65000. The spectrum was collected with 2 s integration time. PL spectroscopy was performed on HZO grown on Au substrate since oxygen vacancy related defect state was more pronounced.

AuNP plasmon resonances were characterized by scattering spectra. High angle and white light sample illumination was done through a × 100 0.8-NA (LPMlanFLN) objective. The AuNPs were identified with a diffraction-limited image using a Lumenera Infinity 2 camera. The dark-field light was sent to the Ocean Optics QE65000 spectrometer. The intensity of scattered light was measured with 10 s integration time.

Cantilever Contacting: Cantilever tips (SD-qp-CONT-TL from Apex Probes) were prepared with thermal evaporation of 3/6 nm of Cr/Au providing transparent conductive tips. Tips were integrated with the microscopy apparatus and positioned on a custom mount operated by XYZR piezoelectric positioners (MCS-6CC RS232 with 6SSF from SmartAct). Pressure on the gap region was 0.037 GPa (discussed in Supporting Information section (h)) due to the cantilever spring constant, k = 0.01 Nm^{-1} (as measured during manufacturing). The

cantilever was lowered via a piezo-controlled actuator until it makes parallel contact with the sample surface. The cantilever remains fixed at this position for the duration of the measurements. The pressure induced on the gap does not modify the switching mechanism as reported in Ref. [32].

Simulation: The plane wave pseudopotential code CASTEP[48] was used for the DFT calculations of HZO's geometry, electronic, and optical properties. OptaDOS[49] was used to post-process the calculated properties from CASTEP to obtain the density of states and dielectric functions of HZO. The far-field scattering spectra and near-field distributions used the DFT dielectric functions as input and were calculated by a commercial simulator based on the FDTD technique (Lumerical Inc., https://www.lumerical.com/products/). Computational details can be found in sections d of the supporting information.

Supporting Information

Supporting Information is available from the Wiley Online Library or from the author.

Conflict of Interest

The authors declare no conflict of interest.

Data Availability Statement

The data that support the findings of this study are openly available in Apollo at https://doi.org/10.17863/CAM.91195, reference number 6319126.

[1] M. T. Tyszkiewicz, S. Daggett, *A Defense Budget Primer*, Library of Congress Washington DC Congressional Research Service, Washington DC **1998**.

[2] J. R. Anderson, *Trans. Am. Inst. Electr. Eng., Part 1* **1953**, *71*, 395.

[3] T. Mikolajick, S. Slesazeck, M. H. Park, U. Schroeder, *MRS Bull.* **2018**, *43*, 340.

[4] V. Garcia, M. Bibes, *Nat. Commun.* **2014**, *5*, 4289.

[5] J. F. Scott, L. Kammerdiner, M. Parris, S. Traynor, V. Ottenbacher, A. Shawabkeh, W. F. Oliver, *J. Appl. Phys.* **1988**, *64*, 787.

[6] A. Grigoriev, D.-H. Do, D. M. Kim, C.-B. Eom, B. Adams, E. M. Dufresne, P. G. Evans, *Phys. Rev. Lett.* **2006**, *96*, 187601.

[7] A. Chanthbouala, V. Garcia, R. O. Cherifi, K. Bouzehouane, S. Fusil, X. Moya, S. Xavier, H. Yamada, C. Deranlot, N. D. Mathur, M. Bibes, A. Barthélémy, J. Grollier, *Nat. Mater* **2012**, *11*, 860.

[8] Z.-D. Luo, X. Xia, M.-M. Yang, N. R. Wilson, A. Gruverman, M. Alexe, *ACS Nano* **2020**, *14*, 746.

[9] H. Joh, M. Jung, J. Hwang, Y. Goh, T. Jung, S. Jeon, *ACS Appl. Mater. Interfaces* **2022**, *14*, 1326.

[10] W. Wu, K. H. Wong, C. L. Choy, *Appl. Phys. Lett.* **2004**, *85*, 5013.

[11] W. J. Merz, *Phys. Rev.* **1954**, *95*, 690.

[12] J. Müller, T. S. Böscke, U. Schröder, S. Mueller, D. Bräuhaus, U. Böttger, L. Frey, T. Mikolajick, *Nano Lett.* **2012**, *12*, 4318.

[13] M. Hyuk Park, H. Joon Kim, Y. Jin Kim, T. Moon, C. Seong Hwang, *Appl. Phys. Lett.* **2014**, *104*, 072901.

[14] U. Schroeder, E. Yurchuk, J. Müller, D. Martin, T. Schenk, P. Polakowski, C. Adelmann, M. I. Popovici, S. V. Kalinin, T. Mikolajick, *Jpn. J. Appl. Phys.* **2014**, *53*, 08LE02.

[15] M. Hoffmann, U. Schroeder, T. Schenk, T. Shimizu, H. Funakubo, O. Sakata, D. Pohl, M. Drescher, C. Adelmann, R. Materlik, A. Kersch, T. Mikolajick, *J. Appl. Phys.* **2015**, *118*, 072006.

[16] S. J. Kim, D. Narayan, J.-G. Lee, J. Mohan, J. S. Lee, J. Lee, H. S. Kim, Y.-C. Byun, A. T. Lucero, C. D. Young, S. R. Summerfelt, T. San, L. Colombo, J. Kim, *Appl. Phys. Lett.* **2017**, *111*, 242901.

[17] T.-H. Ryu, D.-H. Min, S.-M. Yoon, *J. Appl. Phys.* **2020**, *128*, 074102.

[18] Q. Chen, Y. Zhang, W. Liu, J. Jiang, Q. Yang, L. Jiang, *Int. J. Mech. Sci.* **2021**, *212*, 106828.

[19] T. Mikolajick, U. Schroeder, *Nat. Mater.* **2021**, *20*, 718.

[20] M. Pešić, F. P. G. Fengler, L. Larcher, A. Padovani, T. Schenk, E. D. Grimley, X. Sang, J. M. LeBeau, S. Slesazeck, U. Schroeder, T. Mikolajick, *Adv. Funct. Mater.* **2016**, *26*, 4601.

[21] S. Starschich, S. Menzel, U. Böttger, *J. Appl. Phys.* **2017**, *121*, 154102.

[22] F. P. G. Fengler, M. Hoffmann, S. Slesazeck, T. Mikolajick, U. Schroeder, *J. Appl. Phys.* **2018**, *123*, 204101.

[23] Y. Zhou, Y. K. Zhang, Q. Yang, J. Jiang, P. Fan, M. Liao, Y. C. Zhou, *Comput. Mater. Sci.* **2019**, *167*, 143.

[24] P. Jiang, Q. Luo, X. Xu, T. Gong, P. Yuan, Y. Wang, Z. Gao, W. Wei, L. Tai, H. Lv, *Adv. Electron. Mater.* **2021**, *7*, 2000728.

[25] S. R. C. McMitchell, S. Clima, N. Ronchi, K. Banerjee, U. Celano, M. Popovici, L. Di Piazza, G. Van den Bosch, J. Van Houdt, *Appl. Phys. Lett.* **2021**, *118*, 092902.

[26] V. Mukundan, S. Consiglio, D. H. Triyoso, K. Tapily, M. E. McBriarty, S. Schujman, K. Beckmann, J. Hazra, V. Kaushik, N. Cady, R. D. Clark, G. J. Leusink, A. C. Diebold, *Phys. Status Solidi* **2021**, *218*, 2100024.

[27] P. Nukala, M. Ahmadi, Y. Wei, S. de Graaf, E. Stylianidis, T. Chakraborty, S. Matzen, H. W. Zandbergen, A. Björling, D. Mannix, D. Carbone, B. Kooi, B. Noheda, *Science* **2021**, *372*, 630.

[28] K. Lee, K. Park, H.-J. Lee, M. S. Song, K. C. Lee, J. Namkung, J. H. Lee, J. Park, S. C. Chae, *Sci. Rep.* **2021**, *11*, 6290.

[29] Y.-J. Lin, C.-Y. Teng, S.-J. Chang, Y.-F. Liao, C. Hu, C.-J. Su, Y.-C. Tseng, *Appl. Surf. Sci.* **2020**, *528*, 147014.

[30] "Reversible transition between the polar and antipolar phases and its implications for wake-up and fatigue in HfO2-based ferroelectric thin film | Nature Communications," https://www.nature.com/articles/s41467-022-28236-5, n.d.

[31] E. D. Grimley, T. Schenk, X. Sang, M. Pešić, U. Schroeder, T. Mikolajick, J. M. LeBeau, *Adv. Electron. Mater.* **2016**, *2*, 1600173.

[32] G. Di Martino, A. Demetriadou, W. Li, D. Kos, B. Zhu, X. Wang, B. de Nijs, H. Wang, J. MacManus-Driscoll, J. J. Baumberg, *Nat. Electron.* **2020**, *3*, 687.

[33] G. Di Martino, S. Tappertzhofen, S. Hofmann, J. Baumberg, *Small* **2016**, *12*, 1334.

[34] D. Kos, H. P. A. G. Astier, G. D. Martino, J. Mertens, H. Ohadi, D. De Fazio, D. Yoon, Z. Zhao, A. Kuhn, A. C. Ferrari, C. J. B. Ford, J. J. Baumberg, *Small* **2018**, *14*, 1801599.

[35] J. J. Baumberg, J. Aizpurua, M. H. Mikkelsen, D. R. Smith, *Nat. Mater.* **2019**, *18*, 668.

[36] A. Demetriadou, J. M. Hamm, Y. Luo, J. B. Pendry, J. J. Baumberg, O. Hess, *ACS Photon.* **2017**, *4*, 2410.

[37] S. J. Kim, J. Mohan, H. S. Kim, S. M. Hwang, N. Kim, Y. C. Jung, A. Sahota, K. Kim, H.-Y. Yu, P.-R. Cha, C. D. Young, R. Choi, J. Ahn, J. Kim, *Materials* **2020**, *13*, 2968.

[38] M. H. Park, Y. H. Lee, H. J. Kim, Y. J. Kim, T. Moon, K. D. Kim, J. Müller, A. Kersch, U. Schroeder, T. Mikolajick, C. S. Hwang, *Adv. Mater.* **2015**, *27*, 1811.

[39] I. Fina, L. Fàbrega, E. Langenberg, X. Martí, F. Sánchez, M. Varela, J. Fontcuberta, *J. Appl. Phys.* **2011**, *109*, 074105.

[40] A. G. Chernikova, M. G. Kozodaev, D. V. Negrov, E. V. Korostylev, M. H. Park, U. Schroeder, C. S. Hwang, A. M. Markeev, *ACS Appl. Mater. Interfaces* **2018**, *10*, 2701.

[41] J. Y. Lee, G. Anoop, H. J. Lee, J. H. Kwak, J. Y. Jo, *Curr. Appl. Phys.* **2017**, *17*, 704.

[42] M. Kracklauer, F. Ambriz-Vargas, G. Kolhatkar, B. Huber, C. Schindler, A. Ruediger, *Adv. Mater. Lett.* **2019**, *10*, 405.

[43] C.-Q. Luo, C.-Y. Kang, Y.-L. Song, W.-P. Wang, W.-F. Zhang, *Appl. Phys. Lett.* **2021**, *119*, 042902.

[44] Z. Fan, J. Chen, J. Wang, *J. Adv. Dielect.* **2016**, *06*, 1630003.

[45] S. Papernov, M. D. Brunsman, J. B. Oliver, B. N. Hoffman, A. A. Kozlov, S. G. Demos, A. Shvydky, F. H. M. Cavalcante, L. Yang, C. S. Menoni, B. Roshanzadeh, S. T. P. Boyd, L. A. Emmert, W. Rudolph, *Opt. Express OE* **2018**, *26*, 17608.

[46] M. D. Glinchuk, A. N. Morozovska, A. Lukowiak, W. Stręk, M. V. Silibin, D. V. Karpinsky, Y. Kim, S. V. Kalinin, *J. Alloys Compd.* **2020**, *830*, 153628.

[47] N. Kongsuwan, A. Demetriadou, M. Horton, R. Chikkaraddy, J. J. Baumberg, O. Hess, *ACS Photon.* **2020**, *7*, 463.

[48] S. J. Clark, M. D. Segall, C. J. Pickard, P. J. Hasnip, M. I. J. Probert, K. Refson, M. C. Payne, *Z. Kristallogr. – Cryst. Mater.* **2005**, *220*, 567.

[49] A. J. Morris, R. J. Nicholls, C. J. Pickard, J. R. Yates, *Comput. Phys. Commun.* **2014**, *185*, 1477.